Research Square

Preprints are preliminary reports that have not undergone peer review.
They should not be considered conclusive, used to inform clinical practice,
or referenced by the media as validated information.

Integrated coherent LiDAR with broadband low-noise-laser-driven, multidimensionally multiplexed passive beam steering

Linjie Zhou
ljzhou@sjtu.edu.cn
Shanghai Jiao Tong University https://orcid.org/0000-0002-2792-2959
Siyu E
Shanghai Jiao Tong University https://orcid.org/0000-0003-0833-9319
Qiqi Yuan
Shanghai Jiao Tong University
Yuyao Guo
Shanghai Jiao Tong University https://orcid.org/0000-0002-5356-7188
Xinhang Li
Shanghai Jiao Tong University
Chang Li
Shanghai Jiao Tong University
Weihan Xu
Shanghai Jiao Tong University https://orcid.org/0000-0001-5266-3656
Minhui Jin
Shanghai Jiao Tong University
yanyang zhou
Henan Key Laboratory of Quantum Information and Cryptography
Yu Li
Shanghai Jiao Tong University https://orcid.org/0009-0001-5886-5870
Liangjun Lu
Shanghai Jiao Tong University https://orcid.org/0000-0002-6036-5103
Wan-Su Bao
Henan Key Laboratory of Quantum Information and Cryptography https://orcid.org/0009-0003-0226-2944
Jianping Chen
Shanghai Jiaotong University

Article

Keywords:

Posted Date: August 18th, 2026

DOI: https://doi.org/10.21203/rs.3.rs-10675886/v1

License: This work is licensed under a Creative Commons Attribution 4.0 International License.
Read Full License

Additional Declarations: There is **NO** Competing Interest.

Integrated coherent LiDAR with broadband low-noise-laser-driven, multidimensionally multiplexed passive beam steering

***Siyu E*[†]*, Qiqi Yuan*[†]*, Yuyao Guo*[*]*, Xinhang Li, Chang Li, Weihan Xu, Minhui Jin, Yanyang Zhou*[*]*, Yu Li, Liangjun Lu, Wansu Bao, Jianping Chen, and Linjie Zhou*[*]**

[†]These authors contributed equally

[*]Corresponding authors

Affiliations

State Key Laboratory of Micro-Nano Engineering Science, School of Integrated Circuits, Shanghai Jiao Tong University, Shanghai 200240, China.

Siyu E, Qiqi Yuan, Chang Li & Xinhang Li

State Key Laboratory of Photonics and Communications, School of Integrated Circuits, Shanghai Jiao Tong University, Shanghai 200240, China.

Yuyao Guo, Weihan Xu, Minhui Jin, Yu Li, Liangjun Lu, Jianping Chen & Linjie Zhou

SJTU-Pinghu Institute of Intelligent Optoelectronics, Pinghu 314200, China.

Yuyao Guo, Minhui Jin, Yu Li, Liangjun Lu, Jianping Chen & Linjie Zhou

Henan Key Laboratory of Quantum Information and Cryptography, IEU, Zhengzhou 450001, China.

Yanyang Zhou & Wansu Bao

Corresponding author

Correspondence to: guoyuyao1992@sjtu.edu.cn, zyy@qiclab.cn, ljzhou@sjtu.edu.cn

Abstract

Frequency-modulated continuous-wave (FMCW) LiDAR is a promising route towards chip-scale three-dimensional sensing, but its scalability is constrained by two coupled bottlenecks: the control complexity of beam-steering devices, such as active optical phased arrays, and the difficulty of combining wide wavelength tuning with the low-frequency noise required for precise coherent ranging. Here we report a hybrid integrated coherent LiDAR architecture that combines a self-injection-locked external-cavity laser (SILECL) with a multidimensionally multiplexed passive dispersive optical phased array. The laser separates broadband wavelength selection from linewidth compression, providing a 66-nm tuning range and sub-100-Hz intrinsic linewidth across the tuning window, with a minimum linewidth of 50 Hz. The passive emitter uses slanted gratings, bidirectional excitation, and polarization multiplexing to enable 16-fold spectral reuse; when characterized with an external 184-nm wavelength sweep, it demonstrates a 110° × 90° field of view. In FMCW ranging experiments using the SILECL, self-injection locking improves the sweep linearity to above 99.9% and reduces the ranging precision from 8.39 cm to 0.97 cm at 2.1 m. These results highlight a co-design principle for coherent LiDAR, in which source coherence, wavelength agility and passive spatial multiplexing are jointly optimized to reduce beam-steering complexity.

Introduction

Frequency-modulated continuous-wave (FMCW) light detection and ranging (LiDAR) is an attractive approach for chip-scale three-dimensional sensing because it provides not only spatial information but also coherent ranging and velocity readout with high sensitivity[1]. As integrated photonics moves towards compact systems with reduced size, weight, and power, fully solid-state beam steering has become a central requirement for practical FMCW LiDAR[2]. Active optical phased arrays (OPAs) offer a route to electronic beam control, but their scalability is increasingly constrained by the large number of phase shifters, high power consumption, and thermal crosstalk that accompany high element counts[3]. These limitations become particularly severe when a wide field of view and high angular resolution are required simultaneously.

Passive wavelength-steered OPAs provide an alternative architecture in which beam steering is achieved by spectral tuning rather than by driving large numbers of active phase shifters[4]. This approach can greatly

simplify control and reduce electrical overhead, making it appealing for scalable solid-state LiDAR. However, it transfers the system burden to the optical source. In FMCW operation, the laser must support a sufficiently wide tuning range to cover a large angular span, while also maintaining low frequency noise and high chirp linearity to preserve coherent ranging precision[5]. These requirements are difficult to satisfy simultaneously. Moreover, in conventional passive dispersive OPAs, each wavelength is typically mapped to only one resolvable spatial point. The finite spectral bandwidth of any practical laser therefore limits not only the accessible field of view, but also the spatial sampling capacity of the scanner[6]. Current integrated laser architectures do not readily resolve this coupled constraint. Self-injection-locked (SIL) lasers can achieve hertz-level linewidths and excellent coherence, but their tuning range is typically too limited for large-angle wavelength-steered scanning[7,8]. External-cavity lasers (ECLs), by contrast, can provide much broader tuning ranges, but generally with higher frequency noise and less favourable FMCW ranging performance[9,10]. On the beam-steering side, passive dispersive OPAs face a separate trade-off among field of view, beam quality, and spectral efficiency. Designs that improve fill factor and suppress grating lobes often compress the alias-free angular range, whereas architectures with broader steering range can use spectral bandwidth inefficiently. As a result, a scalable fully solid-state FMCW LiDAR requires advances at both levels: a swept source that combines broadband tunability with high coherence, and a passive steering architecture that converts finite spectral bandwidth into a substantially larger number of resolvable spatial channels.

Here we report a hybrid integrated coherent LiDAR architecture that addresses these constraints by combining a self-injection-locked external-cavity laser (SILECL) with a multidimensionally multiplexed passive two-dimensional dispersive OPA. In the laser, a tunable Sagnac loop (TSL) controls the operating state so that broadband wavelength selection is provided by the external cavity, while linewidth compression is preserved through self-injection locking. In the emitter, slanted grating sub-arrays, bidirectional excitation, and polarization multiplexing are combined to increase the number of resolvable angular channels supported by a given tuning bandwidth, thereby overcoming the conventional one-wavelength–one-spot mapping. Using this approach, we obtain a tuning range of 66 nm together with an

intrinsic linewidth of 50 Hz. The passive steering architecture provides a 16-fold increase in spectral resource utilization and a field of view of 110° × 90°. In FMCW operation, the system achieves 99.92% sweep linearity and more than eightfold improved free-space ranging precision compared with the non-SIL state. These results establish a photonic architecture in which a broadband low-noise swept source and passive spectral beam steering can be co-designed for scalable solid-state coherent LiDAR.

Results

1. Integrated coherent LiDAR architecture

Our integrated coherent LiDAR combines a SILECL with a purely passive two-dimensional dispersive OPA to address the coupled limitations of swept-source coherence and solid-state beam steering. As shown in Fig. 1, the laser provides the spectrally agile and low-noise optical carrier required for FMCW ranging, whereas the passive emitter maps wavelength into two-dimensional beam deflection without relying on large arrays of actively driven phase shifters. This architecture therefore separates two functions that are often difficult to optimize simultaneously in conventional systems: broadband wavelength selection is implemented in the external cavity, while linewidth compression is maintained through self-injection locking. At the same time, the passive OPA is designed to use the available tuning bandwidth more efficiently by distributing the spectral resource across multiple angular channels. Together, these elements establish a system-level route to fully solid-state coherent LiDAR that reduces control complexity while preserving the coherence needed for precise ranging.

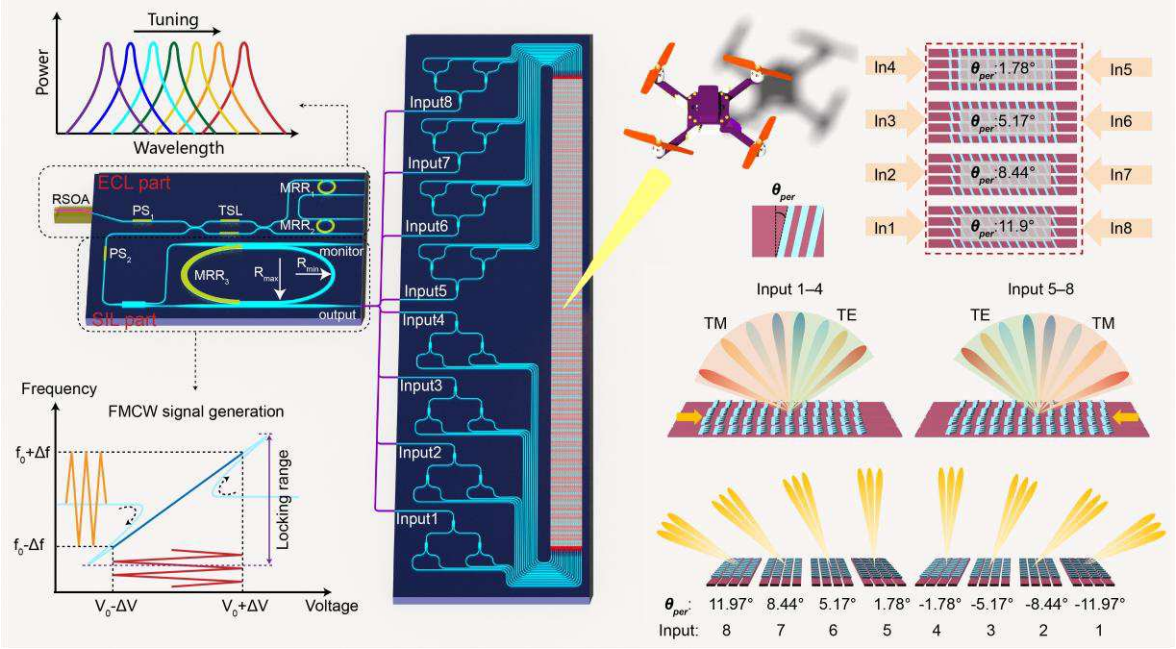


Fig. 1: Architecture and principle of the fully solid-state LiDAR.

The SILECL consists of a reflective semiconductor optical amplifier (RSOA) hybrid-integrated with a silicon nitride (Si_3N_4) photonic chip, which is functionally divided into an ECL section and an SIL section (Fig. 1, left). For broadband wavelength selection, the ECL part incorporates two microring resonators (MRR_1 and MRR_2) operating as a Vernier filter to provide a wide free spectral range (FSR), alongside a TSL that regulates the cavity feedback (Fig. 1, left top). To achieve strong linewidth compression, a portion of the ECL part power is directed into the SIL part, which features a high Q-factor (Q) MRR_3 utilizing Euler bends[11] and a phase shifter (PS_2). By tuning PS_2 to establish phase-aligned resonant feedback, the laser is partly injected back into the RSOA cavity, locking the lasing mode and markedly suppressing frequency noise.

Crucially, this SILECL architecture decouples broadband wavelength selection from linewidth stabilization during FMCW operation. As schematically illustrated in Fig. 1 (left bottom), a triangular voltage ramp applied to the heater of MRR_3 thermally drives a linear shift in its resonance frequency. The laser operates within the self-injection locking range; the lasing mode is continuously pulled and rigidly locked to this

moving resonance, generating a highly linear triangular frequency chirp. While the Vernier filter dictates the wavelength across a wide spectral window, the self-injection locking mechanism simultaneously clamps the dynamic phase noise throughout the frequency sweep. This hybrid configuration yields an exceptionally low frequency noise floor, which drastically enhances the signal-to-noise ratio (SNR) of the beat signal and the ranging precision.

At the emission aperture, to fully harness the wavelength tunability and thus enhance the field of view (FOV), the system employs a multi-dimensional multiplexed purely passive OPA architecture that substantially circumvents the complex electrical driving overhead of traditional active arrays. As shown in Fig. 1, the passive OPA employs a multi-dimensional multiplexing strategy to systematically expand its FOV. Specifically, slanted grating sub-arrays and bi-directional inputs are synergized to multiply the horizontal steering range, while polarization multiplexing between the TE and TM modes is leveraged to extend the longitudinal FOV. This multidimensional multiplexing strategy allows the same wavelength to be reused across multiple input ports, propagation directions, and polarization channels, thereby increasing the number of addressable angular sectors supported by a finite tuning bandwidth.

2. SILECL for broadband low-noise FMCW operation

A central requirement of wavelength-steered FMCW LiDAR is a laser source that supports both wide spectral tuning and sufficiently low frequency noise for coherent distance measurement. These requirements are usually difficult to reconcile in integrated swept sources because designs that favour broad tuning often do so at the expense of frequency noise and chirp stability. In our SILECL, the external cavity defines the wavelength-selective operating window, whereas self-injection locking stabilizes the lasing mode and suppresses phase noise, extending its stabilization efficacy from the static state into active frequency sweeping. This configuration is intended to preserve the tuning flexibility needed for large-angle passive steering while maintaining the spectral purity required for high-fidelity FMCW operation. As summarized in Fig. 2, the source exhibits a broad tuning range together with strong linewidth compression

and improved sweep linearity, indicating that the usual compromise between tunability and coherence can be substantially relaxed in this architecture.

The Si_3N_4 chip was fabricated by LIGENTEC in the standard multi-project wafer (MPW) process. The SILECL was packaged, as depicted in Fig. 2a. To transition between the SIL and non-SIL operating states, the TSL's reflectivity (R_t) was controlled by adjusting the applied currents to the Mach-Zehnder interferometer (MZI) arms. By operating in the non-SIL state (total reflection), the output laser wavelength could be conveniently determined through the monitor port. In this state, the maximum tuning range of the SILECL was achieved by tuning the heaters of MRR_1 and MRR_2. As illustrated in Fig. 2c, the laser wavelength was tuned from 1544 nm to 1610 nm, covering a range of 66 nm, which is comparable to the Vernier filter's FSR. Crucially, simultaneous adjustment of PS_1 was required to ensure precise phase matching. The light-current-voltage (L-I-V) characteristics and the side mode suppression ratio (SMSR) are detailed in the Supplementary Note 1.

After selecting a target wavelength, R_t was adjusted to ~30% to achieve optimal frequency noise compression in the SIL state (Methods provides more details). It is also noted that increasing R_t reduces the intrinsic linewidth in the non-SIL state ($\Delta\nu_{ECL}$) due to the reduction in cavity facet loss. Therefore, in the experiment, the R_t was appropriately increased based on the theoretical calculation to achieve the optimal intrinsic linewidth in the SIL state ($\Delta\nu_{SIL}$). At 1570 nm, we aligned the peak of MRR_3 with the Vernier resonance and adjusted PS_2 to achieve phase matching for the SILECL's compound cavity. In Fig. 2d, the optical frequency noise spectra show that the narrowest intrinsic linewidth achieved was approximately 50 Hz in the SIL state. When MRR_3 was detuned from the Vernier resonance peak, the intrinsic linewidth broadened to approximately 1.2 kHz due to the loss of locking. The integral linewidth in SIL and non-SIL can be calculated to be 10.5 kHz and 30 kHz, respectively[12]. Crucially, the SIL state leads to a frequency noise reduction of two orders of magnitude in the mid-to-low frequency noise range compared to the non-SIL state, a significant improvement for FMCW ranging. To demonstrate the linewidth compression effect across the entire tuning range, the intrinsic linewidths were measured and calculated in

both the SIL and non-SIL states at 5 nm intervals. As presented in Fig. 2e, in the SIL state, the linewidth consistently remained below 97 Hz across the entire tuning range, compared to the non-SIL state linewidth below 1330 Hz.

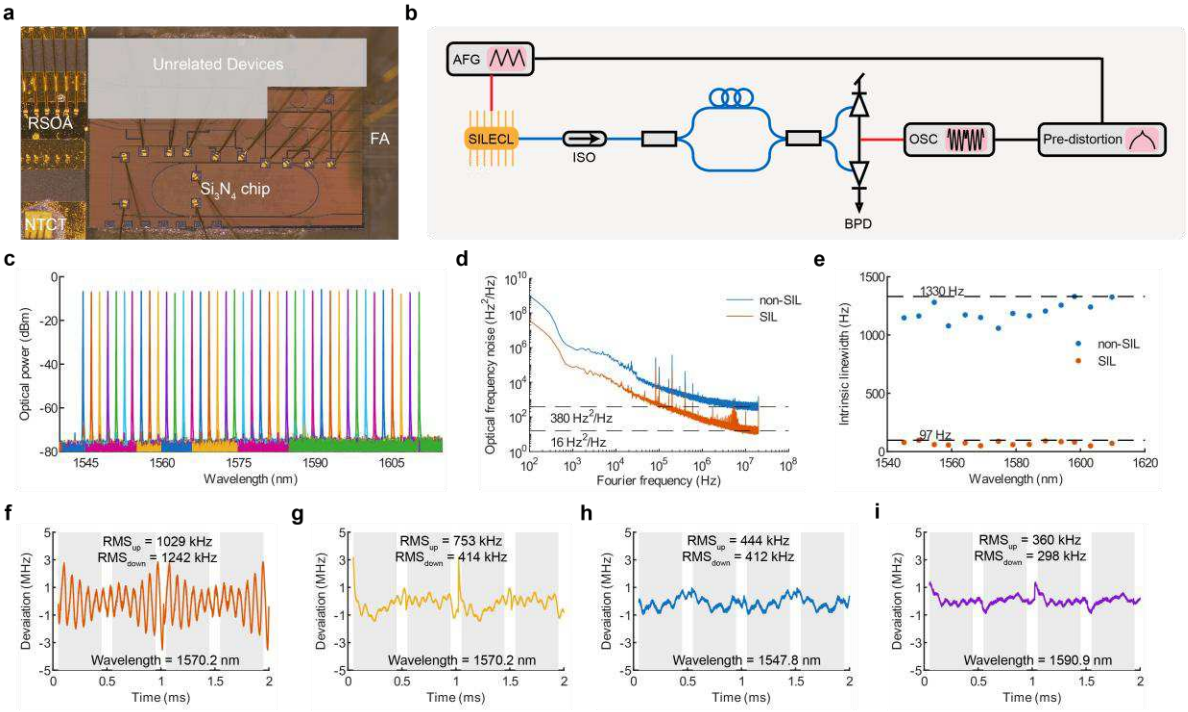


Fig. 2: Performance characterization of the SILECL. a Microscope image of packaged SILECL. **b** Schematic of the driving signal pre-distortion scheme for improving chirp linearity. ISO, isolator; OSC, oscilloscope; BPD, balanced photodetector. **c** Tunable lasing spectra of SILECL. **d** Optical frequency noise spectra of SILECL in the SIL state and non-SIL state. **e** Intrinsic linewidth of SILECL through the entire tuning range in the SIL state and non-SIL state. **f, g, h, i** RMS of the residual frequency error of the up-chirps and down-chirps for the FMCW signals at different wavelengths in non-SIL (**f**) and SIL state (**g, h, i**). The gray background represents the ROI.

A comparative experiment was conducted to verify the impact of the reduced optical frequency noise in the SIL state on the FMCW signal performance. In the non-SIL state, the FMCW signal was generated by

applying a pre-distorted triangular signal to PS_1. The SIL state was achieved by allowing the laser to pass through MRR_3, with the output strictly aligned with its filtering peak. The pre-distortion system is illustrated in Fig. 2b (Methods provides more details). The arbitrary function generator (AFG) sweep rate was maintained at 1 kHz. The region of interest (ROI) was defined as the central 90% of both the up-ramp and down-ramp. To comprehensively evaluate the chirping quality after pre-distortion, we analyzed the linearity, the nonlinearity metric ($1 - R^2$, where R^2 is the linear regression coefficient[13]), and the root mean square (RMS) of the residual frequency error[10]. The quantitative FMCW performance for both the non-SIL and SIL states at different wavelengths is summarized in Table 1 and Fig. 2f–i. In the non-SIL state, the pre-distorted signal exhibited a baseline linearity exceeding 99.8%. As shown in the results, after transitioning to the SIL state, the linearity uniformly exceeded 99.9% across all tested wavelengths (Supplementary Note 3), systematically enhancing the waveform fidelity. Consistently, the SIL state yielded a substantial reduction in both the $1 - R^2$ nonlinearity and the RMS residual frequency errors for both sweep directions. This confirms that the self-injection locking reduces dynamic frequency fluctuations within the tested chirp conditions, improving the coherence and linearity of the optical sweep used for ranging.

Table 1 Summary of FMCW signal characteristics in non-SIL and SIL states.

Operating State	Wavelength (nm)	Ramp Direction	Linearity	Nonlinearity ($1 - R^2$)	RMS Error (kHz)
Non-SIL	1570.2	Up	> 99.8%	3.21×10^{-5}	1029
		Down		4.68×10^{-5}	1242
SIL	1547.8	Up	> 99.9%	1.83×10^{-5}	444
		Down		1.62×10^{-5}	412

SIL	1570.2	Up Down	> 99.9%	6.08×10^{-5} 1.94×10^{-5}	753 414
SIL	1590.9	Up Down	> 99.9%	1.89×10^{-5} 1.35×10^{-5}	360 298

3. Passive two-dimensional steering with spectral multiplexing

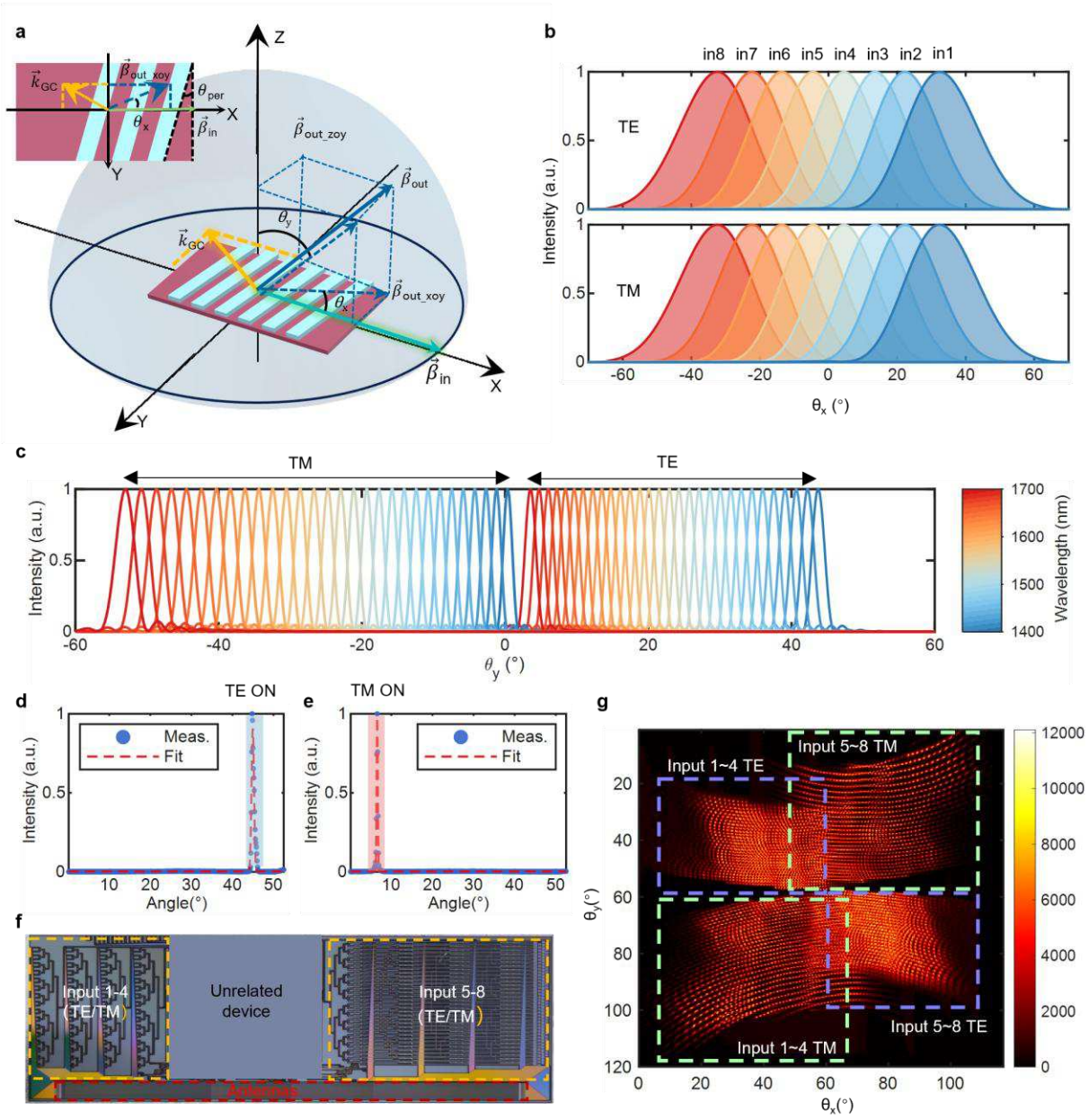


Fig. 3: Architecture of the passive two-dimensional dispersive OPA. a Wave-vector diagrams illustrating the Bragg phase-matching conditions of the slanted grating in three dimensions and two dimensions. **b** Simulated far-field profiles in the horizontal direction (θ_x) for incident TE and TM modes. The grating perturbation tilt angles are configured to -11.97°, -8.44°, -5.17°, -1.78°, 1.78°, 5.17°, 8.44°, and 11.97°, corresponding sequentially to the physical excitation from Input 1 through Input 8. The waveguide width is fixed at 5 μm. **c** Simulated longitudinal far-field diffraction angles as a function of wavelength for

the TE and TM modes. The sub-array with a grating tilt angle of 1.78° is shown as a representative example. **d,e** Far-field measurement results of polarization multiplexing and mode suppression. Measured far-field profiles under (d) TM mode and (e) TE mode incidence. The input wavelength is fixed at 1548.268 nm, and the sub-array with a grating tilt angle of 5.17° is shown as a representative example. **f** Microscope image of the fabricated OPA chip. **g** Measured 2D far-field beam steering point cloud obtained using an external wavelength sweep from 1456 nm to 1640 nm, demonstrating the intrinsic FOV of the passive multidimensional multiplexing emitter.

To simultaneously satisfy the stringent requirements of low propagation loss, minimal phase error, and high emission dispersion efficiency, the entire OPA is designed on Si_3N_4-on-SOI platform. To achieve high-resolution scanning, the system employs long-grating antennas requiring extremely weak coupling strengths. This is achieved by placing the periodic perturbations in the Si_3N_4 layer rather than directly etching the underlying Si waveguide. Concurrently, the bottom Si waveguide is moderately widened to further mitigate random phase errors induced by sidewall roughness. Horizontally, a high fill-factor design (~0.91) is adopted to maximize the main-lobe energy ratio and suppress grating lobes. FDTD simulations indicate that this configuration maintains a main-lobe energy ratio of 68% and a grating lobe suppression ratio (GLSR) exceeding 8 dB (Methods provides more details). Although this high fill-factor inevitably enlarges the grating pitch and restricts the aliasing-free FOV of a single sub-array, this fundamental drawback is effectively circumvented by the proposed multi-dimensional multiplexing architecture.

To maximize spectral resource utilization and expand the FOV, the system synthesizes three distinct multiplexing mechanisms (Supplementary Note 4). First, as illustrated in Fig. 3a, the slanted grating architecture rotates the perturbation vector (θ_{per}) away from the incident axis to freely steer the diffraction vector within a two-dimensional space. By employing four sets of sub-arrays with different slant angles, the horizontal main lobe is pre-steered into four distinct spatial sectors (4-fold expansion). Second, bi-directional injection into these sub-arrays mirrors the effective perturbation angle, doubling the horizontal

scanning range (2-fold). Finally, polarization multiplexing leverages the distinct effective refractive indices of the TE and TM modes to excite independent longitudinal scanning trajectories (2-fold). In terms of addressable wavelength-to-angle channels, the combination of four slanted sub-array sectors, two propagation directions, and two polarization states provides a nominal $4 \times 2 \times 2 = 16$-fold reuse of the same wavelength resource compared with a single-sector, single-polarization passive dispersive emitter, as shown in Fig. 3 b. Here, spectral reuse denotes the number of distinct angular sectors that can be addressed using the same optical wavelength through different passive spatial, directional, or polarization channels. This multidimensional mapping allows the passive structure to use spectral bandwidth more efficiently than conventional one-wavelength-one-spot architectures, while preserving fully solid-state operation and avoiding the control burden of active phase tuning.

To systematically verify the multi-dimensional framework and evaluate the inherent spatial scanning capacity of the passive OPA, optical testing was initially conducted using an external broadly tunable laser. As illustrated in Fig. 3 f & g, the passive OPA architecture integrates eight input ports across four distinct grating sub-arrays to systematically partition and reconstruct the entire emission space. When light is coupled through Inputs 1-4 (located on the left side of the grating groups), the pure TE mode naturally maps to the upper-left quadrant of the far field. Crucially, because the slanted grating configuration alters the radiation vector without perturbing the intrinsic grating pitch, a seamless and high-fidelity stitching across adjacent sub-arrays is achieved. Simultaneously, the TM mode from the same left-side inputs constitutes the lower-left quadrant. By exploiting bi-directional excitation via Inputs 5–8 on the right side, the corresponding TE and TM modes symmetrically reconstruct the lower-right and upper-right quadrants, respectively. Driven by an external broadly tunable laser over 1456-1640 nm, the passive OPA demonstrates a synthesized 2D FOV of $110° \times 90°$. This measurement characterizes the intrinsic spatial coverage of the multidimensional multiplexing emitter. When driven by the 66-nm SILECL, the same wavelength-to-angle mapping mechanism is expected to access a proportionally smaller but still broad angular span, limited by the available source tuning range. As shown in Fig. 3d & e, to firmly support this multi-dimensional operation, polarization isolation—a critical metric for multiplexing fidelity—exhibits a

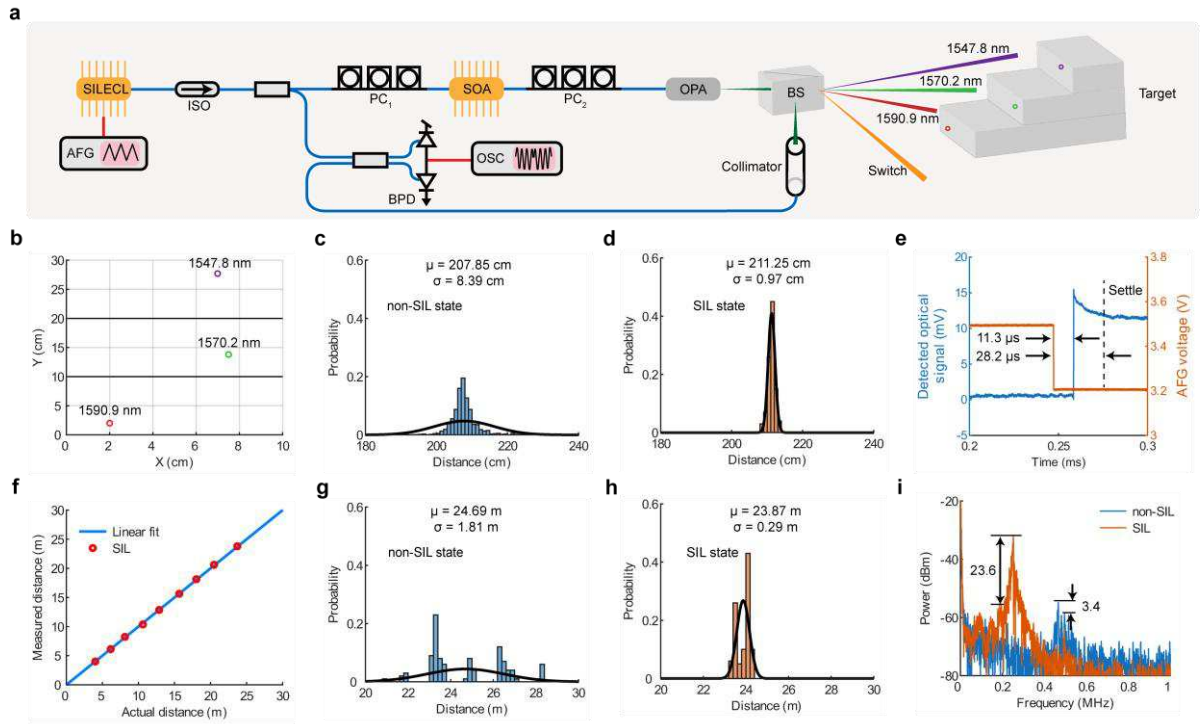
mode extinction ratio exceeding 30 dB across the entire scanning range (limited by the measurement system's noise floor). This high isolation rigorously ensures minimal crosstalk between the dual longitudinal trajectories.

Angular performance was quantitatively evaluated across all sub-arrays. In the horizontal dimension (θ_x), the beam divergence is mode-independent at 0.6°, governed by the 176 μm effective aperture. The horizontal angular dispersion efficiencies are measured at 2.864°/nm for the TE mode and 2.635°/nm for the TM mode. These values are dictated by the delay line network, where the optical path increases sequentially by a constant difference (ΔL = 170.5 μm). The discrepancy in the horizontal dispersion coefficients between the two orthogonal polarizations stems from their distinct effective refractive indices within the waveguide. In the longitudinal dimension (θ_y), the TE mode exhibits divergence angles ranging from 0.044° to 0.054° across different slanted sub-arrays. Compared to the expected performance of a 1.4-mm-long grating aperture, these divergence angles are noticeably larger, which is attributed to phase errors from waveguide thickness non-uniformity. The TM mode exhibits a larger longitudinal divergence (~0.17°) due to stronger grating perturbations. The longitudinal dispersion efficiencies are measured at 0.135°/nm (TE) and 0.156°/nm (TM), with the discrepancy arising from the distinct wave vector magnitudes of the two modes. These results confirm that the integrated architecture successfully translates spectral bandwidth into high-fidelity spatial coverage.

4. Coherent ranging performance of the integrated system

To evaluate the practical implications of the integrated architecture, we operate the system in the FMCW regime and measure its ranging characteristics in free space. In this mode, ranging precision depends jointly on the quality of the optical chirp and the stability of wavelength-to-angle mapping in the passive emitter. The SILECL is designed to improve these conditions by providing a more coherent and more linear swept waveform than the non-self-injection-locked state, while the passive OPA maintains deterministic beam addressing over the scanned field. To validate the compatibility between the SILECL and the passive

dispersive emitter, we performed a proof-of-concept free-space FMCW ranging experiment using three wavelength-addressed beam positions. The experimental setup is depicted in Fig. 4a (Methods provides more details). A stepped structure was employed as the target, with the bottom step located 2 m away from the dispersion chip, and each step possessing a uniform height and width of 10 cm. By tuning the input wavelength, the 2D dispersion chip steers the output beam across three distinct angular positions, precisely illuminating three spots on a staircase-shaped target positioned at different distances and heights, as shown in Fig. 4b. The reconstructed target positions are consistent with the spatial profile captured by the infrared camera at the output of the 2D dispersion chip. To quantitatively assess the free-space ranging precision, 100 consecutive measurements were recorded for each target spot. When operating in the non-SIL state at 1570.2 nm, the ranging precision on the central step was evaluated to be $\sigma = 8.39$ cm (the standard deviation of multiple measurements), with a measured average distance of $\mu = 207.85$ cm (Fig. 4c). In stark contrast, activating the SIL state at the same wavelength significantly improved the precision to $\sigma = 0.97$ cm, yielding an over 8-fold enhancement (Fig. 4d). Following this, the ranging precisions for the upper (1547.8 nm) and lower (1590.9 nm) steps were measured to be 1.25 cm and 0.66 cm, respectively (Supplementary Note 6).



287

288 **Fig. 4: Performance characterization of FMCW LiDAR system. a** Schematic of the experimental setup.
289 SOA, semiconductor optical amplifier; PC, polarization controller; PBS, plate beamsplitter. **b** Spatial
290 coordinates of the incident laser beams at different wavelengths on the target. **c,d** Histograms of 100
291 consecutive distance measurements, demonstrating the ranging precision in the non-SIL state (c) and the
292 SIL state (d) at a range of 2.1 m. **e** Measured temporal waveforms. The orange and blue traces represent the
293 AFG driving voltage applied to the MRR_2 heater and the detected optical response. **f** Measured range versus
294 actual range, illustrating the ranging accuracy for SIL state. **g,h** Histograms of 100 consecutive distance
295 measurements, demonstrating the ranging precision in the non-SIL state (g) and the SIL state (h) at a range
296 of 23.7 m. **i** Frequency spectra of the corresponding beat signals for a target located at 23.7 m under both
297 the non-SIL and SIL states.

298

299 In conventional active OPA-based LiDAR systems, 2D beam steering typically relies on massive arrays of
300 on-chip active phase shifters. Scaling these systems to achieve high-resolution imaging inherently
301 introduces overwhelming driving complexity, as hundreds of individual phase control elements must be

precisely and synchronously modulated. Consequently, even employing intrinsically fast modulation mechanisms—such as the electro-optic effect in silicon or thin-film lithium niobate (TFLN)—the overall dynamic beam steering speed remains severely bottlenecked at the microsecond regime[14]. This system-level limitation arises from the formidable electrical driving overhead of large-scale arrays: synchronously switching thousands of parallel high-speed voltage channels demands massive arrays of digital-to-analog converters (DACs), enormous data throughput, and complex electrical interconnections, severely limiting the practical steering agility.

By avoiding phase shifters in the aperture, the passive OPA reduces the number of electrical control channels required for beam steering; in the present implementation, dynamic addressing is transferred to wavelength tuning and input-port/polarization selection. By fully offloading the spatial steering process from the massive emission part to the driving laser, the dynamic temporal response of the system becomes exclusively dependent on the single-point wavelength agility of the SILECL source. To evaluate the dynamic beam steering performance of our LiDAR system, a temporal response measurement was conducted based on the experimental setup illustrated in Fig. 4a (Methods provides more details). As depicted in Fig. 4e, the orange and blue traces represent the AFG driving signal and the detected optical response, respectively. Upon receiving an electrical trigger signal, the thermo-optic effect takes approximately 11.3 μs to shift the resonance peak of MRR_2 to the position corresponding to the target laser wavelength, thereby realigning the beam toward the target. Subsequently, following a relaxation period of nearly 17 μs, the received voltage of the PD stabilizes within a 2% tolerance band of its final steady-state value, which indicates that the wavelength switching process—and, by extension, the beam deflection—takes approximately 28.2 μs. In this experiment, the observed beam-deflection time is mainly governed by the thermo-optic tuning response of the SILECL heaters.

To demonstrate the long-range measurement capability of the LiDAR architecture, the target was progressively moved from 4 m to 23.7 m for free-space ranging. The deviation between the measured and actual distances is presented in Fig. 4f. At the maximum range of 23.7 m, the system was evaluated under both non-SIL and SIL states. In the non-SIL state, the measured distance exhibited a deviation of ~1 m;

conversely, in the SIL state, this deviation was significantly reduced to merely ~9 cm. Fig. 4g and Fig. 4h illustrate the ranging precision of the two states at 23.7 m. In the SIL state, a ranging precision of 29 cm was recorded, representing an over six-fold enhancement compared to the non-SIL state. The precision degradation at 23.7 m, compared to that at 2.1 m, is mainly attributed to the reduced received optical power and the corresponding decrease in beat-note SNR in the free-space link. Nevertheless, as displayed in the frequency spectra of the corresponding beat signals at 23.7 m (Fig. 4i), self-injection locking increases the beat-note SNR from 5.4 dB to 20.5 dB, indicating that the laser frequency-noise reduction remains beneficial in the long-range regime.

Taken together, these results demonstrate that the co-design of a low frequency noise swept-wavelength source with a passive multidimensional beam-steering architecture offers a practical and scalable photonic pathway toward fully solid-state, chip-scale coherent LiDAR systems.

Discussion

Table 2 compares representative silicon-photonic LiDAR and beam-steering demonstrations. Rather than optimizing a single metric, our work combines three features that are rarely demonstrated together: a broadly tunable sub-100-Hz-linewidth integrated swept source, multidimensional passive spectral reuse, and free-space FMCW ranging through the passive emitter. While traditional ECLs are restricted by kHz-level linewidths and SIL schemes based on DFB lasers remain strictly confined to sub-nanometer tuning, the SILECL successfully bridges this long-standing physical gap. Furthermore, compared to recent purely passive OPAs that suffer from severe FOV compression and a mere 1× spectral reuse factor, our multi-dimensional multiplexing architecture not only pushes the limits of spatial scanning capability but also delivers superior ranging precision during system-level tests, paving the way for next-generation, high-fidelity 3D sensing. Looking ahead, several avenues exist for further enhancing the performance of the SILECL and the overall system.

Table 2 Comparison with representative silicon-photonic LiDAR and beam-steering demonstrations

Laser architecture	Beam steering system	Free-space ranging precision	Divergence angle	FOV	Reuse dimension	Spectral reuse	Ref.
Commercial DFB laser	Thermo-optic OPA + Wavelength	2 cm @ 2 m	0.85°×0.18°	46°×36°	N/A	N/A	[15]
Commercial tunable laser	Purely passive OPA delay lines	N/A	0.16°×0.13°	22.9°×9.2°	1	1	[16]
Commercial tunable laser	Passive OPA (AWG-assisted and different pitch)	N/A	0.24°×0.16°	15°×11.2°	2	32	[17]
Integrated SIL laser	Mechanical Galvo	0.4 cm @ 6.2 m	N/A	N/A	N/A	N/A	[18]
Integrated ECL and EO comb	Passive grating (Vertical) and Mechanical Galvo (Horizontal)	0.9 cm @ 3 m	0.012°	12.23°×8.36°	1	1	[19]
Tapered diode laser	Thermo-optic OPA	N/A	4.1°×0.6°	15°×N/A	N/A	N/A	[20]
Integrated ECL	Active OPA	N/A	0.051°×0.016°	140°×16°	1	1	[21]
Integrated SILECL	Passive multidimensional OPA (Bi-dir + Pol. + Slanted)	0.97 cm @ 2 m	0.6°×0.05°（TE） 0.6°×0.17°（TM）	110° × 90° (external 184-nm sweep)	3	16×	This work

Note: Values are taken from the cited reports and may correspond to different measurement conditions. For this work, the 110° × 90° FOV refers to passive OPA characterization using an external 184-nm wavelength sweep, whereas the FMCW ranging experiments were performed using the integrated SILECL at selected wavelengths.

The FOV can be enhanced from two complementary directions: the light source and the emission side. On the source side, the tuning range can be further extended beyond 100 nm by increasing the Vernier FSR[9]. Meanwhile, the incorporation of broadband couplers effectively mitigates insertion losses and enhances the uniformity of the sweeping performance across a wide spectral range[22]. A wider tuning range would greatly benefit applications such as OPA by enabling larger scanning angles[9,21]. On the emission side, the demonstrated 110° × 90° passive-emitter FOV indicates that multidimensional spectral reuse can support wide-angle beam steering. Our multi-dimensional multiplexing strategy remains highly scalable. Should nearly hemispherical coverage be required, the spatial scanning range could be further expanded by integrating additional slanted sub-arrays or using multiple grating pitches, although this would require careful management of insertion loss, sector overlap, and beam quality. Crucially, this slanted-grating approach inherently averts the severe beam degradation that typically plagues conventional OPAs at extreme steering angles.

Channel scaling from a single driving source to multiple emission sub-arrays provides an additional route for system optimization. In the current proof-of-concept experiment, different sub-array sectors are addressed by fiber routing and polarization selection. This implementation was chosen to isolate and validate the passive emitter physics. In a scalable system, these addressing functions could be implemented using integrated optical switches, polarization management circuits, or parallel transceiver channels. Importantly, such addressing circuitry is separate from the emission aperture and does not require dense phase-shifter arrays across the OPA aperture. Furthermore, because each slanted sub-array covers a non-overlapping spatial sector, the architecture supports a parallel transceiver configuration via optical power splitting. This parallelized scheme enables concurrent data acquisition across multiple quadrants of the FOV, increasing both imaging throughput and frame rate without adding complexity to the laser source.

Beyond FOV expansion, further optimizing the system's angular resolution fundamentally relies on enlarging the effective optical aperture. In the proposed architecture, the horizontal angular resolution can be straightforwardly improved by scaling up the number of array elements. Conversely, enhancing the

longitudinal angular resolution hinges on advancing the fabrication processes. Specifically, tightening the thickness uniformity of the waveguide layer is crucial to minimizing accumulated phase errors along the long-grating antennas, thereby allowing the longitudinal divergence to approach its theoretical diffraction limit.

Looking ahead, the system's capabilities can be further elevated through coordinated algorithmic and hardware scaling. To fully exploit the SILECL's locking capacity, future implementations can incorporate synchronous pre-distortion across PS_2 and MRR_3, establishing real-time phase matching to systematically expand the active chirp bandwidth[13] (Supplemental Note 2). Furthermore, optimizing the cavity design by scaling up the MRR_3 perimeter and lowering its coupling coefficient (κ_3^2) offers a reliable pathway. Modelling suggests that further reduction of frequency noise and improved chirp-bandwidth utilization could support millimetre-scale precision over longer ranges (Methods). To unlock next-generation frame rates, transitioning to ultrafast electro-optic (EO) modulation—such as integrating lithium niobate ($LiNbO_3$) MRRs—presents a compelling roadmap[23,24]. This acceleration inherently immunizes the system against low-frequency noise to bolster the ranging SNR, while seamlessly translating into an agile beam-steering velocity for high-frame-rate 3D imaging.

The system integration can be further enhanced. Beyond reducing electrical driving complexity, the purely passive nature of the proposed OPA provides a crucial process-compatibility advantage for monolithic integration. Integrating essential magneto-optical (MO) circulators typically requires high-temperature thermal annealing (~800°), which catastrophically degrades the active components in conventional OPAs.

In contrast, our dielectric-only, passive emission aperture exhibits inherent thermal robustness, ensuring seamless compatibility with MO material processing. This establishes a viable physical foundation for monolithically integrating a tunable driving laser, an MO circulator, and a wide-FOV OPA onto a single photonic chip[25].

In summary, with its 110° × 90° field of view, fully solid-state architecture, and low electrical control complexity, we envision our integrated LiDAR system providing transformative solutions across a range of emerging applications. By completely offloading the spatial steering process from massive arrays of active phase shifters to a single tunable laser, this passive 2D dispersive OPA framework substantially reduces the system's overall size, weight, and power (SWaP) [26,27]. For practical deployment, the absence of dense active components minimizes power consumption and simplifies thermal management, removing major engineering barriers to widespread commercialization. Consequently, the architecture is particularly well-suited for highly constrained platforms, such as micro-unmanned aerial vehicles (UAVs) and swarm robotics, where the high power requirements of conventional active OPAs are prohibitive[3,27].

Furthermore, this architecture enables a fundamental physical decoupling of the active and passive regions. Because the emission aperture is purely passive, the transceiver chip can be connected to the SILECL source and processing units via a single thin optical fiber, facilitating highly flexible distributed deployment. In automotive LiDAR, for instance, this design allows the ultra-compact passive antenna to be seamlessly integrated directly onto the vehicle's windshield, circumventing the massive surface area typically occupied by current mainstream roof-mounted systems. Concurrently, the ~~volume-intensive~~ laser module and data processing units can be securely housed in the vehicle's chassis or trunk. Finally, the dielectric-only nature of the passive emission aperture exhibits inherent thermal robustness. This unique physical resilience opens pathways for deployment in extreme environments, including aerospace and satellite-to-satellite coherent sensing, where traditional active components often suffer from severe thermal crosstalk or catastrophic degradation[28–30].

Materials and methods

Impact of Linewidth Reduction on FMCW Ranging

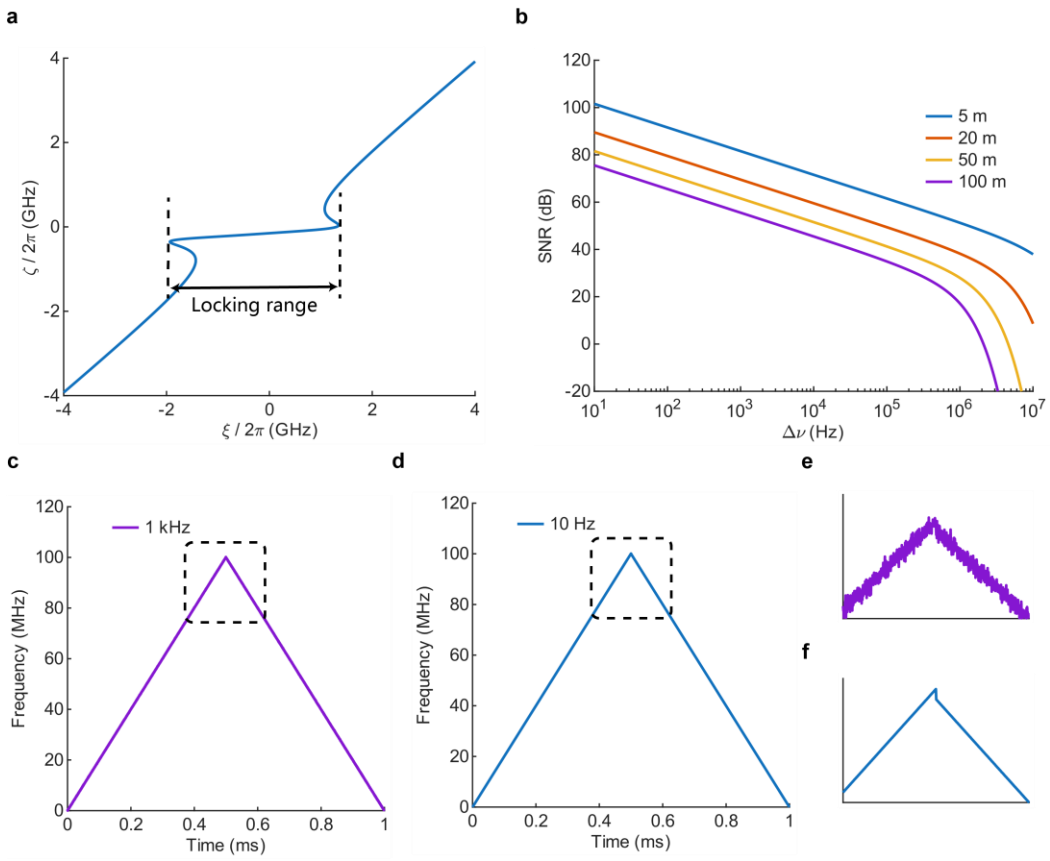
Once in the SIL state, the angular frequency detuning of the ECL part (ξ), induced by factors such as temperature drifts, is significantly suppressed. More specifically, the relationship between the ξ and the output frequency detuning of the SILECL (ζ) can be derived by (Supplementary Note 2):

$$\xi = \zeta + \kappa_s\left[\alpha_g \cos\left(\phi_{eff}\right) + \sin\left(\phi_{eff}\right)\right] \quad (1)$$

where $\xi = \omega_e - \omega_m$ and $\zeta = \omega_s - \omega_m$. Here, ω_e, ω_s, and ω_m denote the output angular frequency in the non-SIL state, the output angular frequency in the SIL state, and the resonant angular frequency of MRR_3, respectively. α_g is the linewidth enhancement factor, κ_s is the feedback coefficient, ϕ_{eff} is the phase of the effective reflectivity of the SIL part. The detuning curve in the SIL state (Extended Data Fig. 1a) can be plotted using equation (1) to illustrate the locking range (Δf_{lr}) and the slope within this range. The inverse of the slope, also referred to as the stabilization factor (K), can be used to calculate the intrinsic linewidth after locking[31]:

$$\Delta\nu_{SIL} = \Delta\nu_{ECL}/K^2 \quad (2)$$

With $R_t \approx 30\%$, the linewidth is calculated to decrease by a factor of ~100, and the Δf_{lr} is estimated to be ~3.4 GHz (see Supplementary Note 2 for specific data).



Extended Data Fig. 1: Theoretical analysis of the SILECL. a The detuning curve of SILECL in the SIL state. **b** SNR of the FMCW signal in relation to linewidth for various ranges. **c, d** Comparison of the output FMCW signals in the time domain from lasers with different laser linewidths. **e, f** Magnified views providing closer examination of the corresponding regions shown in **c** and **d**, respectively.

The advantages of the SILECL over a classical ECL are particularly evident in FMCW LiDAR systems. Range precision, which represents the ability to precisely measure a static target, is typically quantified by σ of multiple measurements[10]. In practical ranging applications, the frequency noise and B of the FMCW signal play a determinant role in the ranging precision of the system. The lower bound of ranging precision can be derived from the Cramer-Rao Lower Bound (CRLB)[32]:

$$\sigma \geq \frac{c}{4\pi B}\sqrt{\frac{1}{SNR\left(1+\frac{1}{SNR}\right)}} \quad (3)$$

where the SNR can be expressed as[33]:

$$SNR = 10 \cdot \lg\left\{\frac{T}{\tau_c}\left[e^{2\tau/\tau_c} - \left(1 + \frac{2\tau}{\tau_c}\right)\right]^{-1}\right\} \quad (4)$$

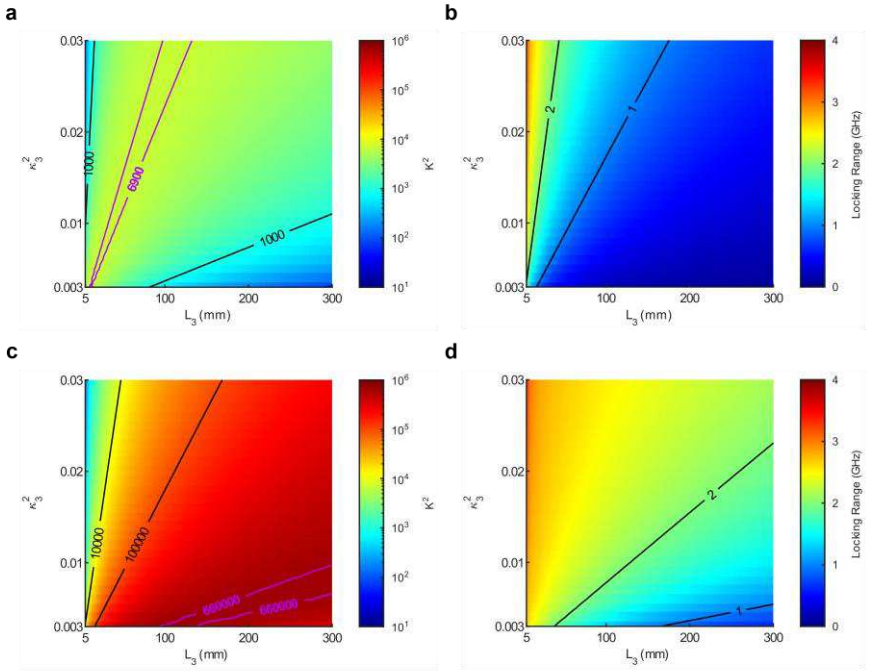
where T is the frequency sweep period (set to 1 ms), $\tau_c = \frac{1}{\pi \cdot \Delta\nu}$ is the limit coherence time of the laser, $\Delta\nu$ is the intrinsic linewidth of the laser, $\tau = \frac{2D}{c}$ is the round-trip time of the FMCW signal, and D is the ranging distance. Based on equation (4), the difference in SNR for FMCW signals generated by lasers with varying linewidths at the same ranging distance can be analyzed, as shown in Extended Data Fig. 1b. At a ranging distance of 100 m, the SNRs for FMCW signals with linewidths of 1 kHz, 100 Hz, and 10 Hz are ~55 dB, ~68 dB and ~75 dB, respectively. Assume B remains unchanged, substituting a 26 dB SNR improvement into equation (3) reveals that the corresponding ranging precisions are enhanced by ~20-fold.

To intuitively illustrate the effects of laser linewidth, a Cauchy distribution model is employed[34]. And the FMCW signal linearity of 99.9% is simulated by a parabolic distortion model[34]. Extended Data Fig. 1c and d show the frequency-versus-time waveforms of the FMCW signal under different linewidths, while Extended Data Fig. 1e and f present the corresponding enlarged views. It can be observed that as the laser linewidth decreases from 1 kHz to 10 Hz, the chirp signal exhibits significantly reduced distortion. This is consistent with the broadening of the full width at half maximum (FWHM) of the beat signal in the frequency domain.

Furthermore, iterative optimization of the SILECL parameters can theoretically further improve both the ranging precision and B. Based on the theoretical derivations in Supplementary Note 2, increasing the circumference of MRR_3 (L_3) while reducing the power coupling coefficients of the MRR_3 (κ_3^2) leads to a maximum K^2 value above 6900 (Extended Data Fig. 2a), accompanied by a gradual narrowing of the locking range (Extended Data Fig. 2b). This limitation on K^2 is primarily attributed to the waveguide power transmission loss in MRR_3 (α_3) at 3 dB/m. Furthermore, reducing α_3 to 0.3 dB/m can significantly boost K^2 to above 6.6×10^5 while maintaining a locking range exceeding 1 GHz (Extended Data Fig. 2c and d). Under these conditions, equation (2) predicts that $\Delta\nu_{SIL}$ can be reduced to ~2 mHz. Such ultra-low loss

476 Si_3N_4 waveguides can be achieved through geometry optimization, such as increasing the waveguide width
477 or employing thin Si_3N_4 layers[7]. Based on Equations (3) and (4), and assuming a sweep rate of 1 kHz over
478 a 100 m distance, the ranging precision is expected to improve by a factor of ~775. Consequently, compared
479 to the experimental ranging precision of 100 m fiber link in the non-SIL state, the SIL state is estimated to
480 achieve a precision of ~5 mm. Additionally, synchronous modulation and pre-distortion algorithms applied
481 to PS_2 and MRR_3 can further optimize the utilization of the locking range[13].

482



483

484 **Extended Data Fig. 2: Dependence of calculated K^2 and locking range on the structural parameters**
485 **of the SILECL. a** Calculated variation of K^2 as a function of L_3 and κ_3^2 with $\alpha_3 = 0.3\,dB/m$. **b**
486 Calculated variation of locking range as a function of L_3 and κ_3^2 with $\alpha_3 = 0.3\,dB/m$. **c** Calculated
487 variation of K^2 as a function of L_3 and κ_3^2 with $\alpha_3 = 3\,dB/m$. **d** Calculated variation of locking range as
488 a function of L_3 and κ_3^2 with $\alpha_3 = 3\,dB/m$.

489

It should be noted that the above derivations consider only white noise. When low- and mid-frequency noise components are included, the intrinsic linewidth broadens into the integral linewidth. However, compared to the non-SIL state, the SIL state still enables a significant reduction in noise across the entire frequency spectrum[8].

Pre-distortion System and Experimental Setup

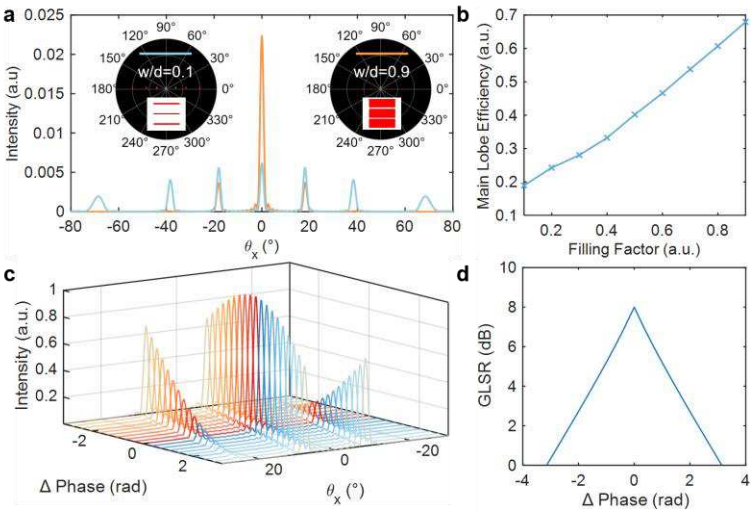
A combination of a non-uniform sampling algorithm and a linear update algorithm is used to pre-distort the driving waveform[13]. The resulting beat signal, obtained from a self-heterodyne system established with a 5 m long fiber, was detected by a BPD. The Hilbert Transform (HT) was then applied to the beat signal to extract its phase information, which in turn allowed for the reconstruction of the laser's frequency chirp.

Free-space ranging was demonstrated using pre-distorted FMCW signals under the self-injection-locked (SIL) state at three distinct wavelengths, while the signal under the non-SIL state was utilized as a benchmark. The pre-distorted FMCW signal was split into two branches by a 50/50 optical coupler. One branch was amplified by a semiconductor optical amplifier (SOA) and routed to the 2D dispersion chip. Subsequently, a 50/50 free-space beam splitter (BS) was employed to facilitate coaxial alignment between the OPA chip and the collimator, enabling precise spatial targeting. The other branch served as the local oscillator (LO). The optical signal reflected from the target was collected, coherently mixed with the LO, and subsequently captured by a balanced photodetector (BPD).

To evaluate the dynamic beam steering performance of our LiDAR system, an AFG was utilized to apply a DC bias of 3.2 V to the micro-heater of MRR_2, tuning the SILECL to a lasing wavelength of 1570.2 nm. The emitted light was subsequently amplified by an SOA and fed into the dispersion chip to steer the beam onto a target located 2 m away. The signal was collected by a collimator and captured by the BPD. When the driving voltage on the MRR_2 heater was increased by 0.3 V, the resultant wavelength hop caused the

steered beam to deviate from the target. Consequently, the reflected light escaped the acceptance angle of the collimator, leading to a zero photocurrent output from the BPD. To dynamically monitor this process, a 1-kHz square-wave driving signal—switching between a low level of 3.2 V and a high level of 3.5 V—was generated by the AFG, and the real-time optical response from the PD was recorded using the OSC.

High Fill-Factor Design and Grating Lobe Suppression



Extended Data Fig. 3: Grating lobe suppression and far-field optimization based on the high fill-factor design. **a** Simulated far-field profiles for fill factor (FF) of 0.1 and 0.9, respectively, at a constant grating array pitch of 5.5 μm. **b** Main lobe energy ratio as a function of the fill factor when the phase difference between adjacent elements is zero. **c, d** Evolution of the far-field diffraction patterns (**c**) and the corresponding grating lobe suppression ratio (GLSR) (**d**) when the inter-element phase difference is continuously tuned from -180° to 180°.

In the design of OPA, suppressing grating lobes and increasing the main lobe energy ratio are crucial for achieving a high SNR in point cloud imaging. However, large-scale OPAs often suffer from reduced aliasing-free FOVs when the element pitch exceeds half a wavelength. To optimize the far-field distribution under such conditions, our proposed system adopts a high fill-factor technical scheme. The array fill factor is defined as the ratio of the width of a single grating waveguide to the grating array pitch.

Detailed numerical analyses were conducted using the three-dimensional finite-difference time-domain (3D-FDTD) method. As illustrated in Extended Data Fig. 3, at a fixed grating array pitch of 5.5 μm, employing a conventional low fill factor (e.g., 0.1) inevitably generates numerous high-intensity grating lobes across the entire FOV. Under this condition, the main lobe energy ratio drastically falls below 20%, which would cause severe aliasing and signal misjudgment in practical LiDAR applications.

Our simulations quantitatively reveal a nearly linear positive correlation between the main lobe energy ratio and the fill factor when the inter-element phase difference is zero. By increasing the fill factor to 0.9, the main lobe energy ratio surges to 68%, representing a significant enhancement of approximately 5.3 dB compared to the 0.1 fill-factor configuration. Furthermore, when the inter-element phase difference is swept from -180° to 180° (using our actual experimental parameters: grating pitch of 5.5 μm and grating width of 5 μm, corresponding to a fill factor of ~0.91), the high fill-factor design consistently maintains a main lobe energy ratio of up to 68% and a grating lobe suppression ratio (GLSR) exceeding 8 dB.

References

1. Royo, S. & Ballesta-Garcia, M. An overview of lidar imaging systems for autonomous vehicles. *Appl. Sci.* **9**, 4093 (2019).
2. Hsu, C.-P. *et al.* A Review and Perspective on Optical Phased Array for Automotive LiDAR. *IEEE J. Sel. Topics Quantum Electron.* **27**, 1–16 (2021).
3. Zhang, X., Kwon, K., Henriksson, J., Luo, J. & Wu, M. C. A large-scale microelectromechanical-systems-based silicon photonics LiDAR. *Nature* **603**, 253–258 (2022).
4. Yu, L. *et al.* Two-Dimensional Beam Scanning of Passive Optical Phased Array Based on Silicon Nitride Delay Line. *J. Lightwave Technol.* **41**, 2756–2764 (2023).
5. Liu, Y. *et al.* High-resolution arrayed waveguide grating-assisted passive optical phased array for 2D beam steering. *Opt. Express* **33**, 7714–7722 (2025).
6. Dostart, N. *et al.* Serpentine optical phased arrays for scalable integrated photonic lidar beam steering. *Optica* **7**, 726–733 (2020).

7. Li, B. *et al.* Reaching fiber-laser coherence in integrated photonics. *Opt. Lett.* **46**, 5201–5204 (2021).
8. Jin, W. *et al.* Hertz-linewidth semiconductor lasers using CMOS-ready ultra-high-Q microresonators. *Nat. Photonics* **15**, 346–353 (2021).
9. Guo, Y. *et al.* Hybrid integrated external cavity laser with a 172-nm tuning range. *APL Photonics* **7**, 66101 (2022).
10. Liu, C. *et al.* Highly-linear and wavelength-tunable frequency-modulated continuous-wave hybrid-integrated laser. *Laser Photonics Rev.* **18**, 2300882 (2024).
11. E, S. *et al.* Stable Microwave Signal Generation by Heterodyning Dual Lasers Injection-Locked to a Single Microring Resonator. *ACS Photonics* **12**, 5133–5143 (2025).
12. Tran, M. A., Huang, D. & Bowers, J. E. Tutorial on narrow linewidth tunable semiconductor lasers using Si/III-V heterogeneous integration. *APL Photonics* **4**, 111101 (2019).
13. Liu, C. *et al.* Hybrid integrated frequency-modulated continuous-wave laser with synchronous tuning. *J. Lightwave Technol.* **40**, 5636–5645 (2022).
14. Ma, X. *et al.* Multi-target and ultra-high-speed optical wireless communication using a thin-film lithium niobate optical phased array. *Nat. Commun.* **17**, 969 (2025).
15. Poulton, C. V. *et al.* Coherent solid-state LIDAR with silicon photonic optical phased arrays. *Opt. Lett.* **42**, 4091–4094 (2017).
16. Hutchison, D. N. *et al.* High-resolution aliasing-free optical beam steering. *Optica* **3**, 887–890 (2016).
17. Muñoz, P. *et al.* Scalable switched slab coupler based optical phased array on silicon nitride. *IEEE J. Sel. Topics Quantum Electron.* **28**, 1–16 (2022).
18. Liu, C. *et al.* Fast-tuning and narrow-linewidth hybrid laser for FMCW ranging. *Laser Photonics Rev.* **19**, 2401338 (2025).
19. Chen, R. *et al.* Integrated bionic LiDAR for adaptive 4D machine vision. *Nat. Commun.* **17**, 24 (2025).
20. Fowler, D. *et al.* SiN optical phased array directly coupled to a high power 905 nm tapered diode laser. *Opt. Express* **33**, 40180–40190 (2025).

21. Xu, W. *et al.* Fully integrated solid-state LiDAR transmitter on a multi-layer silicon-nitride-on-silicon photonic platform. *J. Lightwave Technol.* **41**, 832–840 (2023).
22. Li, D. *et al.* Broadband silicon nitride power splitter based on bent directional couplers with low thermal sensitivity. *Micromachines* **13**, 559 (2022).
23. Wu, Y. *et al.* Combining lithium-niobate and silicon-nitride integrated photonics in ultrafast tunable, low-noise lasers. *Laser Photonics Rev.* **20**, e02207 (2026).
24. Churaev, M. *et al.* A heterogeneously integrated lithium niobate-on-silicon nitride photonic platform. *Nat. Commun.* **14**, 3499 (2023).
25. Yan, W. *et al.* Ultra-broadband magneto-optical isolators and circulators on a silicon nitride photonics platform. *Optica* **11**, 376–384 (2024).
26. Kandil, M., Prost, M., Kjellman, J., Bogaerts, W. & Dahlem, M. Experimental evaluation of continuous and pixelated dispersive optical phased arrays for 2D beam steering. *Photonics Res.* **13**, 1331–1340 (2025).
27. Poulton, C. V. *et al.* Long-range LiDAR and free-space data communication with high-performance optical phased arrays. *IEEE J. Sel. Topics Quantum Electron.* **25**, 1–8 (2019).
28. Boyu, T. *et al.* Review of optical phased array technology and its applications. *High Power Laser Partical Beams* **35**, 41001–22 (2023).
29. Guo, Y. *et al.* Integrated photonics for space communication and sensing. *J. Phys.: Photonics* **7**, 42001 (2025).
30. Milanizadeh, M., Aguiar, D., Melloni, A. & Morichetti, F. Canceling thermal cross-talk effects in photonic integrated circuits. *J. Lightwave Technol.* **37**, 1325–1332 (2019).
31. Laurent, P., Clairon, A. & Breant, C. Frequency noise analysis of optically self-locked diode lasers. *IEEE J. Quantum Electron.* **25**, 1131–1142 (1989).
32. Thurn, K., Ebelt, R. & Vossiek, M. Noise in homodyne FMCW radar systems and its effects on ranging precision. in *2013 IEEE MTT-S International Microwave Symposium Digest (MTT)* 1–3 (2013). doi:10.1109/MWSYM.2013.6697654.

33. Yokota, N., Kiuchi, H. & Yasaka, H. Directly modulated optical negative feedback lasers for long-range FMCW LiDAR. *Opt. Express* **30**, 11693–11703 (2022).
34. Bianconi, S., Ribes-Pleguezuelo, P. & Silvestri, F. Requirements for next-generation integrated photonic FMCW LiDAR sources. *Nat. Commun.* **16**, 6739 (2025).

Acknowledgements

This work was supported in part by the National Natural Science Foundation of China (NSFC) (62135010, 62305212, 62405184, 62120106010), the National Key R&D Program of China (2024YFA1409400), the Natural Science Foundation of Shanghai (24ZR1431400), Quantum Science and Technology-National Science and Technology Major Project (2024ZD0300800), Shanghai 2024 "Science and Technology Innovation Action Plan" Basic Research Project in Integrated Circuit Field (24JD1401600).

Author contributions

Siyu E performed the theoretical analysis and numerical simulations of the SILECL and conducted both the SILECL and FMCW ranging experiments. Qiqi Yuan designed the OPA device structure, performed its theoretical analysis and numerical simulations, and carried out the related experiments. Yuyao Guo proposed the device structure of SILECL. Chang Li assisted with the spatial light ranging experiments. Weihan Xu assisted with the OPA experiments. Xinhang Li assisted with the FMCW experiments. Minhui Jin, Yu Li, Liangjun Lu, Wansu Bao, and Jianping Chen provided valuable suggestions to the project. Yuyao Guo, Weihan Xu, Yanyang Zhou, and Linjie Zhou supervised the project. Siyu E and Qiqi Yuan wrote the manuscript. Siyu E, Qiqi Yuan, Weihan Xu, Yuyao Guo, Yanyang Zhou, and Linjie Zhou revised the manuscript.

Conflict of Interest

The authors declare no conflict of interest.

Supplementary Files

This is a list of supplementary files associated with this preprint. Click to download.

- Supplementaryinformation.docx